

## Polarization in early optical afterglows of gamma-ray bursts driven by precessing jets

BAO-QUAN HUANG<sup>1</sup> AND TONG LIU<sup>1</sup>

<sup>1</sup>*Department of Astronomy, Xiamen University, Xiamen, Fujian 361005, China*

### ABSTRACT

Jet precessions are widely involved in astrophysical phenomena from galaxies to X-ray binaries and gamma-ray bursts (GRBs). Polarization presents a unique probe of the magnetic fields in GRB jets. The precession of GRBs relativistic jets will change the geometry within the observable emitting region of the jet, which can potentially affect the polarization of the afterglow. In this paper, we take into account jet precession to study the polarization evolution and corresponding light curves in GRB early optical afterglows with ordered and random magnetic field geometries. We find that the jet precession in long-lived engines can significantly reduce the polarization degree (PD) regardless of the magnetic field structure. The strongest PD attenuation is found when the line of sight is aligned with the precession axis. Our results show that jet precession can provide new insight into the low PD measured in the early optical afterglows of GRBs.

*Keywords:* Gamma-ray bursts (629); Magnetic fields (994); Polarimetry (1278); Shocks (2086); Relativistic jets (1390)

### 1. INTRODUCTION

The properties of precessing jets have been widely studied in galaxies (see e.g., Miley 1980; Begelman et al. 1984; Lu 1990; Proctor 2011), X-ray binaries such as SS 433 (e.g., Margon 1984), Swift J164449.3+573451 (Burrows et al. 2011), and MAXI J1820+070 (Ma et al. 2021), as well as in gamma-ray bursts (GRBs, see e.g., Blackman et al. 1996; Portegies Zwart et al. 1999; Reynoso et al. 2006; Liu et al. 2010; Sun et al. 2012; Hou et al. 2014; Huang et al. 2019; Huang & Liu 2021).

Being the strongest explosions with  $\gamma$ -ray emission in the Universe, GRBs are believed to be powered by ultra-relativistic jets (see a review by Zhang 2018). GRBs have two types of progenitors, i.e., the coalescence of compact objects and the collapse of massive stars, which correspond to short- and long-duration GRBs (SGRBs and LGRBs), respectively (see the reviews by Woosley & Bloom 2006; Nakar 2007; Liu et al. 2017a). If misalignment in the directions of the angular momenta of merged compact objects or anisotropic collapsars occurs, the new-born compact objects, involving a massive millisecond pulsar (e.g., Usov 1992; Dai & Lu 1998a,b; Zhang & Mészáros 2001; Li et al. 2016; Hou et al. 2021)

and a rapidly rotating and hyperaccreting black hole (for reviews, see Liu et al. 2017a), will power the precessing jets (Liu et al. 2017b). Additionally, precession has been proposed as one of the probable scenarios powering quasi-periodic oscillations during the GRB gamma-ray prompt emission (Tarnopolski & Marchenko 2021).

The multiwavelength afterglow that is usually detected after the short-lived prompt  $\gamma$ -ray emission originates from the synchrotron radiation of electrons accelerated by forward and reverse shocks (FS and RS, respectively), produced when the jets interact with the circumburst medium (e.g., Zhang et al. 2006, and references therein). In this context, the polarimetry of GRB afterglows has become an important topic as it can provide crucial information on the properties of the magnetic fields embedded in the jets (for a review, see Gill et al. 2021). In recent years, a faster response of the GRB detection technology has allowed early-time polarization measurements of several afterglows (e.g., Gorbovskoy et al. 2016; Laskar et al. 2019; Buckley et al. 2021). Currently, the measurements for early optical afterglows show a polarization degree (PD) with a wide range of 1%  $\sim$  30% (e.g., Covino & Gotz 2016; Steele et al. 2017). Different origins have been proposed regarding the PD in this range. The dust from the Galactic interstellar medium or GRB host galaxies (e.g., Jordana-Mitjans et al. 2020) and the magnetic fields produced in the FSs (e.g., King et al. 2014;

Jordana-Mitjans et al. 2021) might result in the low PD. To account for the higher PD ( $> 10\%$ ) measured in RSs, large-scale ordered magnetic fields are thought to be the primary origin, such as GRB 090102 (Steele et al. 2009), GRB 110205A (Steele et al. 2017), and GRB 120308A (Mundell et al. 2013).

It is expected that the large-scale ordered magnetic fields inherited from the central engine remain in the jets (e.g., Spruit et al. 2001; Lazzati 2006), and, hence, a high PD (up to  $\sim 60\%$ ) has been predicted to appear in the early phase of the afterglows (Granot & Königl 2003). However, compared with the maximum theoretically predicted value, most of the measured PD of the early optical afterglows whose jets are suggested to possess large-scale ordered magnetic fields are still substantially low (Rybicki & Lightman 1979; Lyutikov et al. 2003). This means that there are other factors that weaken the PD even if large-scale ordered magnetic fields robustly exist (Zhang & Yan 2011; Deng et al. 2017). For instance, the RSs can be significantly suppressed due to the high magnetization in the jet ejecta (Zhang & Kobayashi 2005; Giannios et al. 2008), and then, high PD is not expected for the early afterglow emission, or a mixed magnetic field structure exists in the jets (Lan et al. 2019a). These factors, in principle, can exist individually or simultaneously. In addition to the magnetic field geometry, the jet structure can also affect the PD (Rossi et al. 2004). Therefore, more scenarios, such as jet precession, should be taken into account to understand the low PD measured in the early optical afterglows of GRBs.

In this paper, we aim to study the effects of jet precession on the polarization evolution of the GRB early afterglows. The paper is arranged as follows: We introduce the jet precession model in Section 2 and the polarization of synchrotron emission in an FS-RS system is calculated in Section 3. The main results are given in Section 4, and a brief summary is given in Section 5.

## 2. DYNAMICS

We employ the treatment used in Huang & Liu (2021) to calculate the afterglow polarization of GRBs produced by the long-lived precessing jets. In this framework, the precession process causes the observer to view an intermittent jet, which we model as a series of subjets.

In the first precession period, owing to the interaction between the subjets and the interstellar medium (ISM, considered here), a pair of relativistic shocks are generated for each subjet, i.e., an FS propagating into the ISM and a RS propagating into the subjet. There are four regions separated by this pair of shocks with a con-

tact discontinuity, including the unshocked ISM (Region 1), the shocked ISM (Region 2), the shocked subjet (Region 3), and the unshocked subjet (Region 4). Among them, Regions 2 and 3 are treated as a system with a uniform Lorentz factor, which decelerates after sweeping in enough ISM. In order for the jet precession to have a significant impact on the overall observed polarization, the active timescale of the central engine needs to be far larger than the precession period, i.e., an energy injection/long-lived engine scenario (Laskar et al. 2015). Consequently, the subsequent subjets in each period catch up with the previous system, leading to energy injection and refreshing of the RS. With increasing ISM mass, the velocity of the system reduces more quickly, hence less time is spent by later subjets to catch up.

### 2.1. Dynamics before RS crossing time

For a long-lasting and magnetized central engine, an extended version of the mechanical model proposed by Beloborodov & Uhm (2006) is employed here to delineate the evolution of the Lorentz factor  $\Gamma$  of the system before the time when the RS passes through the subjet in the last period (i.e., the RS crossing time), which can be obtained by solving the differential equations listed as follows (e.g., Ai & Zhang 2021):

$$\frac{\beta}{r_d^2} \frac{d}{dr_d} (r_d^2 \Sigma \Gamma) - \Gamma [\rho_r (\beta - \beta_r) + \rho_f (\beta_f - \beta)] = 0, \quad (1)$$

$$\begin{aligned} & \frac{\beta}{r_d^2} \frac{d}{dr_d} (r_d^2 \Gamma^2 H \beta) - \Gamma^2 \beta [h_r (\beta - \beta_r) + h_f (\beta_f - \beta)] \\ & + \frac{\beta}{4\pi} \frac{d}{dr_d} (\Gamma^2 \beta \mathcal{B}) + \frac{\beta \Gamma^2}{4\pi} [B_r^2 \beta_r - B_f^2 \beta_f] + (p_f - p_r) \\ & + \frac{\Gamma^2 (1 + \beta^2)}{8\pi} (B_f^2 - B_r^2) + \frac{(1 + \beta^2) \Gamma^2 \mathcal{B}}{4\pi r_d} = 0, \end{aligned} \quad (2)$$

$$\begin{aligned} & \frac{\beta}{r_d^2} \frac{d}{dr_d} (r_d^2 \Gamma^2 H) - \Gamma^2 [h_r (\beta - \beta_r) + h_f (\beta_f - \beta)] \\ & - \beta \frac{dP}{dr_d} - (\beta_r p_r - \beta_f p_f) + \frac{\beta}{8\pi} \frac{d}{dr_d} [(1 + \beta^2) \Gamma^2 \mathcal{B}] \\ & + \frac{(1 + \beta^2) \Gamma^2}{8\pi} (\beta_r B_r^2 - \beta_f B_f^2) + \frac{\Gamma^2 \beta}{4\pi} (B_f^2 - B_r^2) \\ & + \frac{\beta \Gamma^2 \mathcal{B}}{2\pi r_d} = 0, \end{aligned} \quad (3)$$

$$\frac{d\mathcal{B}}{dr_d} = \frac{1}{4\pi r_r^2} \frac{d\mathcal{B}_{\text{sph}}}{dr_d} - 2\mathcal{B} \frac{r_d}{r_r^2}, \quad (4)$$

$$H = \Sigma c^2 + \frac{\hat{\gamma}}{\hat{\gamma} - 1} P. \quad (5)$$

Here,  $\Sigma \equiv \int_{r_r}^{r_f} \rho dr$ ,  $P \equiv \int_{r_r}^{r_f} p dr$ ,  $H \equiv \int_{r_r}^{r_f} h dr$ , and  $\mathcal{B} \equiv \int_{r_r}^{r_f} B^2 dr$ , with  $r_r$ ,  $r_d$ , and  $r_f$  are the distances of

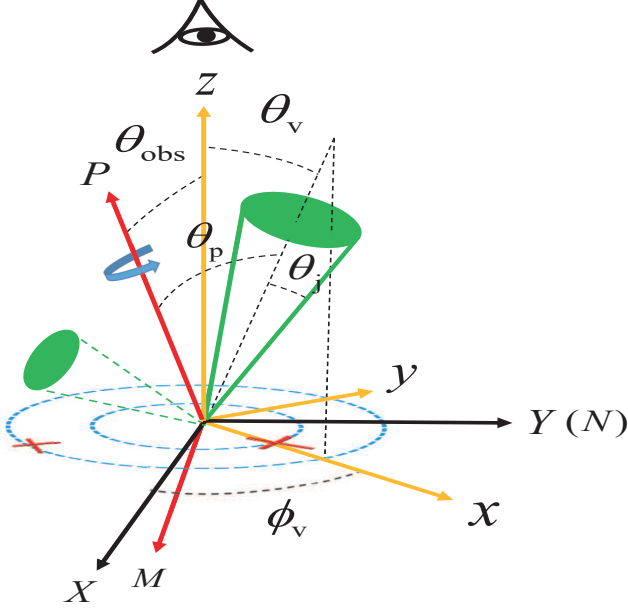


**Figure 1.** Illustration of a GRB precessing jet.

the RS, the contact discontinuity, and the FS from the central engine, which represent the integrated quantities of the mass density, the thermal pressure, the enthalpy, and the square of the magnetic field, respectively.  $\rho_r$  ( $\rho_f$ ),  $p_r$  ( $p_f$ ),  $h_r$  ( $h_f$ ), and  $B_r$  ( $B_f$ ) denote the values of  $\rho$ ,  $p$ ,  $h$ , and  $B$  immediately behind the RS (FS) in the comoving of the system, respectively, which can be acquired by the shock jump condition (e.g., Zhang & Kobayashi 2005).  $\beta_r$ ,  $\beta$ , and  $\beta_f$  are the velocities of the RS, the contact continuity, and the FS in the lab frame, respectively.  $\hat{\gamma}$  is the adiabatic index. In addition,  $\mathcal{B}_{\text{sph}}$  is the integrated quantity of the square of the magnetic field but with an integral over the volume, and its evolution with  $r_d$  can be expressed as  $d\mathcal{B}_{\text{sph}}/dr_d = 4\pi\sigma_r L_{\text{ej}}(\beta_{\text{ej}} - \beta_r)/\Gamma\Gamma_{\text{ej}}\beta\beta_{\text{ej}}c(1 + \sigma_{\text{ej}})$ , where  $L_{\text{ej}}$ ,  $\Gamma_{\text{ej}}$ ,  $\beta_{\text{ej}}$ ,  $\sigma_{\text{ej}}$ , and  $\sigma_r$  are the luminosity of the central engine, the Lorentz factor of the unshocked subjects, the velocity of the unshocked subjects in the lab frame, the magnetization parameter of the unshocked subjects, and the magnetization parameter at the RS downstream, respectively.

The mass of the system contains two parts: the mass of Regions 2 and 3. The mass evolution of these two regions with radius  $r_d$  can be expressed as (e.g., Huang et al. 1999; Nava et al. 2013)

$$dm_2 = 4\pi r_f^2 n_1 m_p dr_f, \quad (6)$$

and

$$dm_3 = 4\pi r_r^2 n_3 m_p \Gamma dX, \quad (7)$$

respectively, where  $dr_f = \beta_f dr_d / \beta$ ,  $dX = (\beta_{\text{ej}} - \beta) dr_d / (\Gamma n_3 / \Gamma_{\text{ej}} n_4 - 1) \beta$ ,  $n_1$ ,  $n_3$ , and  $n_4$  are the number

densities of Regions 1, 3, and 4 in the frame themselves, and  $m_p$  is the proton mass. For convenience, quantities with a prime are defined in the comoving frame.

Adopting a constant Lorentz factor  $\Gamma_{\text{ej}}$  for the unshocked subjects, there exists a scenario where the RS has already passed through the current subject before the next subject catches up. For this situation, we assume that there is not enough time for Regions 2 and 3 to independently evolve between after the RS crosses the current subject and before the next subject catches up and assume that the dynamic evolution of the system during this phase is only dominated by the FS. These assumptions should be reasonable for the case considered in this work given that the precession period is much less than the active timescale of the central engine. On the other hand, we describe the dynamical evolution with the ejection time  $\tau$  of the subjects from the central engine, instead of radius  $r_d$ , which can be achieved by replacing  $dr_d$  with  $d\tau$  in the above equations via the expression

$$dr_d = \begin{cases} \frac{c\beta\beta_{\text{ej}}}{(\beta_{\text{ej}} - \beta_r)} d\tau, & T_{\text{start}} < \tau < T_{\text{end}}, \\ \frac{c\beta\beta_{\text{ej}}}{(\beta_{\text{ej}} - \beta)} d\tau, & \text{others,} \end{cases} \quad (8)$$

where  $T_{\text{start}} = [(i-1)\Delta t + (j-1)T]$ ,  $T_{\text{end}} = [i\Delta t + (j-1)T]$ ,  $i$  ( $= 1, 2, \dots, k$ ) denotes the sequence number of subjects within each period,  $j$  ( $= 1, 2, \dots, t_{\text{end}}/T$ ) represents the sequence number of the precession period,  $T$  is the precession period, and  $\Delta t = T/k$  (Huang & Liu 2021). Moreover, by combining Equation (8) with formula  $dr_d = c\beta dt / (1 - \beta)(1 + z)$ , where  $t$  is the time measured in the observer frame and  $z$  is the redshift, we can derive the relation between differential quantities  $dt$  and  $d\tau$ .

## 2.2. Dynamics after RS crossing time

After the RS crossing time, Regions 2 and 3 begin to evolve independently. For Region 2, the evolution of the Lorentz factor  $\Gamma_2$  can be expressed as (e.g., Chen & Liu 2021)

$$\frac{d\Gamma_2}{dR_2} = -\frac{\Gamma_2^2 - 1}{[\epsilon + 2(1 - \epsilon)\Gamma_2]m_2} \frac{dm_2}{dR_2}, \quad (9)$$

where  $dm_2/dR_2 = 4\pi R_2^2 n_1 m_p dR_2$ , with  $R_2$  being the distance from the central source, and  $\epsilon$  is the fraction of the thermal energy that is radiated, set as zero here. Likewise, for Region 3, the dynamical evolution is described by the Blandford-McKee (BM) self-similar solution in the context of a thick shell. Because of the limitation of the BM self-similar solution, which is only valid in the ultrarelativistic and relativistic phases, our calculation is terminated before entering the nonrelativistic phase.

**Table 1.** Definitions, units, and values of the basic parameters.

Parameters	Definitions	Unit	Values in Case I (II)*
$L_{\text{ej}}$	luminosity of the central engine	erg/s	$10^{49}$
$\Gamma_{\text{ej}}$	Lorentz factor of the unshocked sub-jets		300
$\sigma_{\text{ej}}$	magnetization parameter of the unshocked sub-jets		$10^{-1}$ ( $10^{-3}$ )
$n_1$	number density of the ISM	$\text{cm}^{-1}$	1
$\varepsilon_{e,2}$	fraction of the internal energy density in the FS downstream shared by the electrons		$10^{-1}$
$\varepsilon_{B,2}$	fraction of the thermal energy density in the FS downstream shared by the magnetic field		$10^{-3}$
$p_2$	power-law index of the energy distribution of the shocked electrons in the FS downstream		2.5
$\varepsilon_{e,3}$	fraction of the internal energy density in the RS downstream shared by the electrons		$10^{-1}$ ( $10^{-3}$ )
$a$	power-law index of the ordered magnetic field decaying at Region 3 after the RS crossing time		1
$p_3$	power-law index of the energy distribution of the shocked electrons in the RS downstream		2.5
$T$	precession period of the jets	s	10
$t_{\text{end}}$	age of the jets	ks	1
$\theta_{\text{p}}$	precession angle	degree	7
$\Pi_0$	linear PD for synchrotron emission from a point-like region		0.6
$\delta$	orientation of the aligned magnetic field	rad	$\pi/4$
$\theta_{\text{j}}$	half-opening angle of jets	degree	5
$z$	redshift		1

\* The values of the basic parameters in case II are the same as that in case I and are, therefore, not shown for brevity.

### 3. POLARIZATION

We consider synchrotron radiation as the emission mechanism of the afterglows. For a given frequency  $\nu'$ , the synchrotron radiation power is (Rybicki & Lightman 1979)

$$P'_{\text{syn}}(\nu') = \frac{\sqrt{3}e^3 B' \sin \theta'_B}{m_e c^2} \int_{\gamma'_{e,\min}}^{\gamma'_{e,\max}} \left( \frac{dN'_e}{d\gamma'_e} \right) F\left(\frac{\nu'}{\nu'_c}\right) d\gamma'_e, \quad (10)$$

where  $e$  is the electron charge,  $m_e$  is the electron mass, and  $\theta'_B$  is the pitch angle of the electrons, namely, the angle between the direction of the velocity of the electrons and the direction of the magnetic field  $B'$ .  $F(\nu'/\nu'_c) = (\nu'/\nu'_c) \int_{\nu'/\nu'_c}^{+\infty} K_{5/3}(x) dx$ , with  $K_{5/3}(x)$  being a modified Bessel function of order  $5/3$ , is the synchrotron spectrum function, where  $\nu'_c = 3eB'\gamma_e'^2 \sin \theta'_B / 4\pi m_e c$  is the critical frequency of electrons with Lorentz factor  $\gamma'_e$ .  $\gamma'_{e,\min}$ ,  $\gamma'_{e,\max}$ , and  $dN'_e/d\gamma'_e$  are the minimum, the maximum Lorentz factor, and the energy spectrum of the shock-accelerated electrons, respectively (e.g., Huang & Cheng 2003; Huang & Liu 2021).

In the calculations of the afterglow polarization, two types of magnetic field geometries confined in the shock plane, globally ordered and random, are considered, where globally ordered magnetic fields involve both aligned and toroidal configurations. For simplicity, we assume that the random magnetic field is only generated by the FS and exists in Region 2 and assume that the ordered magnetic field only originates from the magnetic central engine and exists in Region 3 (Sari 1999). Therefore, the random magnetic field is expressed as  $B'_2 = \sqrt{32\pi\Gamma(\Gamma-1)n_1 m_p \varepsilon_{B,2} c^2}$ , with  $\varepsilon_{B,2}$  being the fraction of the thermal energy density in the FS downstream shared by the random magnetic field; note that  $\Gamma$  is replaced by  $\Gamma_2$  in the formula after the RS crossing time. Likewise, the ordered magnetic field can be

solved by the shock jump condition (e.g., Ai & Zhang 2021) before the RS crossing time. Since the evolution of the ordered magnetic field cannot be obtained from the shock jump condition after the RS crossing time, we assume that the ordered magnetic field power law decays with radius, i.e.,  $B'_3 \propto R_3^{-a}$ , with  $R_3$  being the distance of Region 3 from the central source and  $a = 1$  (see Table 1).

Considering an off-axis observer, we initially set a lab frame  $xyz$  with the  $z$  axis aligned with the line of sight and the  $x$  axis oriented along the projected direction of the jet axis moving due to the precession in the plane of the sky, as shown in Figure 1. In this frame,  $\theta_v$  denotes the angle between the line of sight and the jet axis,  $\theta_{\text{j}}$  represents the jet half-opening angle, and the position of a jet element is described as  $(\theta, \phi)$ .

#### 3.1. Stokes parameters in a random magnetic field

In the random magnetic field in Region 2, the local PD of a point-like region with a random magnetic field can be expressed by (e.g., Toma et al. 2009; Lan et al. 2016)

$$\Pi_{\text{p}} = -\Pi_0 \frac{\langle (\sin \theta'_B)^{1-m} \cos(2\phi'_B) \rangle}{\langle (\sin \theta'_B)^{1-m} \rangle}, \quad (11)$$

where  $\cos(2\phi'_B) = (2 \sin^2 \eta' / \sin^2 \theta'_B) - 1$  and  $\sin \theta'_B = (1 - D^2 \sin^2 \theta \cos^2 \eta')^{1/2}$ , with  $D = 1/\Gamma(1 - \beta \cos \theta)$  being the Doppler factor,  $\Pi_0$  is the PD from a smaller region,  $m$  is obtained from the power-law spectrum  $f'_{\nu'} \propto (\nu')^m$  (Sari et al. 1998), and  $\langle \rangle$  represents the average over  $\eta'$  from 0 to  $2\pi$ .

By integrating the flux received from those point-like regions with the same observation time in Region 2, one can calculate the observed flux density as follows:

$$F_{\nu_{\text{obs}},i,2} = \frac{1+z}{4\pi D_L^2} \int_{\theta_-}^{\theta_+} \int_{-\Delta\phi}^{\Delta\phi} P'_{\text{syn}}(\nu') D^3 \sin \theta d\theta d\phi, \quad (12)$$

where subscript “2” represents integration carried out in Region 2,  $\nu' = (1+z)\nu_{\text{obs}}/D$  with  $\nu_{\text{obs}}$  is the observed frequency, and  $D_L$  is the luminosity distance in the stan-

$$\begin{pmatrix} Q_{\nu_{\text{obs}},i,2} \\ U_{\nu_{\text{obs}},i,2} \end{pmatrix} = \frac{1+z}{4\pi D_L^2} \int_{\theta_-}^{\theta_+} \int_{-\Delta\phi}^{\Delta\phi} P'_{\text{syn}}(\nu') \Pi_p D^3 \sin\theta d\theta \begin{pmatrix} \cos(2\phi) \\ \sin(2\phi) \end{pmatrix} d\phi. \quad (13)$$

Here, the corresponding integral limits are (e.g., Wu et al. 2005; Geng et al. 2018)

$$\Delta\phi = \begin{cases} \pi\Theta(\theta_v - \theta_j), & \theta \leq \theta_-, \\ \arccos\left(\frac{\cos\theta_j - \cos\theta_v \cos\theta}{\sin\theta_v \sin\theta}\right), & \theta_- < \theta < \theta_+, \\ 0, & \theta \geq \theta_+, \end{cases} \quad (14)$$

where  $\Theta$  is the Heaviside step function,  $\theta_- = |\theta_j - \theta_v|$ , and  $\theta_+ = \theta_j + \theta_v$ . In addition,  $U_{\nu_{\text{obs}},i,2} (\propto \int \sin(2\phi)d\phi)$  is equal to zero.

$$\begin{pmatrix} Q_{\nu_{\text{obs}},i,3} \\ U_{\nu_{\text{obs}},i,3} \end{pmatrix} = \Pi_0 \frac{1+z}{4\pi D_L^2} \int_{\theta_-}^{\theta_+} \int_{-\Delta\phi}^{\Delta\phi} P'_{\text{syn}}(\nu') D^3 \sin\theta d\theta \begin{pmatrix} \cos(2\chi) \\ \sin(2\chi) \end{pmatrix} d\phi, \quad (16)$$

where subscript “3” represents integration carried out in Region 3 and  $\chi$  is the position angle of the polarization for a point-like region. Here, if the ordered magnetic field exists with an aligned configuration, the position

$$\chi = \phi + \arctan\left(\frac{\cos\theta - \beta}{(1 - \beta \cos\theta)} \frac{\sin\theta_v \sin\phi}{(\cos\theta_v \sin\theta - \sin\theta_v \cos\theta \cos\phi)}\right). \quad (18)$$

Additionally, it should be noted that  $\sin(2\chi)$  is an odd function of  $\phi$  in the toroidal configuration (Spruit et al. 2001), and, hence,  $U_{\nu_{\text{obs}},i,3} \propto \int_{-\Delta\phi}^{\Delta\phi} \sin(2\chi)d\phi = 0$  will always remain in this configuration.

### 3.3. Effects of jet precession

We accumulate the Stokes parameters calculated in each subject at the same observation time to obtain the total polarization effect. Because the Stokes parameters in each subject are acquired in the moving coordinate

standard  $\Lambda$ CDM cosmology model ( $\Omega_M = 0.27$ ,  $\Omega_\Lambda = 0.73$ , and  $H_0 = 71 \text{ km s}^{-1} \text{ Mpc}^{-1}$ ). Additionally, the Stokes parameters,  $Q_{\nu_{\text{obs}},i,2}$  and  $U_{\nu_{\text{obs}},i,2}$ , are given by (e.g., Geng et al. 2018)

### 3.2. Stokes parameters in an ordered magnetic field

In the ordered magnetic field of Region 3, similar to that in the random magnetic field, the observed flux density is given by

$$F_{\nu_{\text{obs}},i,3} = \frac{1+z}{4\pi D_L^2} \int_{\theta_-}^{\theta_+} \int_{-\Delta\phi}^{\Delta\phi} P'_{\text{syn}}(\nu') D^3 \sin\theta d\theta d\phi, \quad (15)$$

and the other two Stokes parameters are

angle can be expressed as (e.g., Lan et al. 2016)

$$\chi = \phi + \arctan\left[\frac{\cos\theta - \beta}{\cos\theta(1 - \beta \cos\theta)} \cot(\phi - \delta)\right], \quad (17)$$

where  $\delta$  is the direction of the aligned magnetic field. If the ordered magnetic field possesses a toroidal configuration, the position angle is given by

system  $xyz$ , we transition the Stokes parameters from the moving coordinate system  $xyz$  to a global coordinate system  $XYZ$  with the  $X$  axis aligned with the projected direction of the precession axis in the plane of the sky, as shown in Figure 1, which can be accomplished by the

rotation matrix (e.g., Lan et al. 2019b), i.e.,

$$\begin{pmatrix} F_{\nu_{\text{obs}},i,j}^X \\ Q_{\nu_{\text{obs}},i,j}^X \\ U_{\nu_{\text{obs}},i,j}^X \end{pmatrix} = \begin{pmatrix} 1 & 0 & 0 \\ 0 & \cos 2\alpha & \sin 2\alpha \\ 0 & -\sin 2\alpha & \cos 2\alpha \end{pmatrix} \begin{pmatrix} F_{\nu_{\text{obs}},i,j} \\ Q_{\nu_{\text{obs}},i,j} \\ U_{\nu_{\text{obs}},i,j} \end{pmatrix}. \quad (19)$$

Here,  $\alpha = 2\pi - \phi_v$  is the rotation angle moving anticlockwise from the  $x$  axis to the  $X$  axis, wherein  $\phi_v$  is the azimuthal angle of the jet axis in the coordinate system  $XYZ$ , and its value can be solved by the following relations:

$$\sin \theta_v \cos \phi_v = \sin \theta_{\text{obs}} \cos \phi_{\text{obs}} \cos \theta_p + \cos \theta_{\text{obs}} \cos \phi_{\text{obs}} \sin \theta_p \cos \phi_p - \sin \phi_{\text{obs}} \sin \theta_p \sin \phi_p, \quad (20)$$

$$\sin \theta_v \sin \phi_v = \sin \theta_{\text{obs}} \sin \phi_{\text{obs}} \cos \theta_p + \cos \theta_{\text{obs}} \sin \phi_{\text{obs}} \sin \theta_p \cos \phi_p + \cos \phi_{\text{obs}} \sin \theta_p \sin \phi_p, \quad (21)$$

$$\cos \theta_v = \cos \theta_{\text{obs}} \cos \theta_p - \sin \theta_{\text{obs}} \sin \theta_p \cos \phi_p, \quad (22)$$

where  $(\theta_{\text{obs}}, \phi_{\text{obs}})$  represents the coordinate of the precession axis in the coordinate system  $XYZ$  and  $(\theta_p, \phi_p)$  denotes the coordinate of the jet axis in the coordinate system  $MNP$  with the  $M$  axis on the  $zX$  plane and  $P$  the precession axis, as shown in Figure 1.

After coordinate transformation, the PD and polarization angle (PA) of the calculated radiation involving the effect of jet precession can be expressed as

$$\Pi^X = \frac{\sqrt{Q_{\nu_{\text{obs}}}^X{}^2 + U_{\nu_{\text{obs}}}^X{}^2}}{F_{\nu_{\text{obs}}}^X}, \quad (23)$$

and

$$\chi^X = \frac{1}{2} \arctan \left( \frac{U_{\nu_{\text{obs}}}^X}{Q_{\nu_{\text{obs}}}^X} \right), \quad (24)$$

respectively, where  $F_{\nu_{\text{obs}}}^X = \sum_i \sum_j F_{\nu_{\text{obs}},i,j}^X$ ,  $Q_{\nu_{\text{obs}}}^X = \sum_i \sum_j Q_{\nu_{\text{obs}},i,j}^X$ , and  $U_{\nu_{\text{obs}}}^X = \sum_i \sum_j U_{\nu_{\text{obs}},i,j}^X$ , with  $j$  ( $= 2, 3$ ) representing the radiating regions.

Notably, the actual value of the PA cannot be acquired only by Equation (24). To determine the real value of the PA, the sign of the Stokes parameters  $U_{\nu_{\text{obs}}}^X$  and  $Q_{\nu_{\text{obs}}}^X$  also need to be considered here. Namely, the real value is equal to  $\chi^X$  if  $Q_{\nu_{\text{obs}}}^X > 0$ , to  $\chi^X + \pi/2$  if  $Q_{\nu_{\text{obs}}}^X < 0$  and  $U_{\nu_{\text{obs}}}^X > 0$ , and to  $\chi^X - \pi/2$  if  $Q_{\nu_{\text{obs}}}^X < 0$  and  $U_{\nu_{\text{obs}}}^X < 0$  (e.g., Lan et al. 2018).

#### 4. RESULTS

We numerically calculate the net linear polarization of the optical afterglows by considering the total contributions of the FS and RS in Regions 2 and 3, respectively,

in two cases, i.e., the ordered magnetic field dominates (Case I) or the random magnetic field dominates (Case II). In our calculations, there is merely a slight dependency of the results across optical wavelengths as shown in Shimoda & Toma (2021), so we only take account of the R-band. We assume a top-hat jet with the half-opening angle  $\theta_j = 5^\circ$ , consider the equal arrival time surface effect, and ignore the lateral expansion effect (e.g., Zhang & MacFadyen 2009; Huang & Liu 2021). The age  $t_{\text{end}}$  of the jet beginning at  $\phi_p = 180^\circ$  is set as 1 ks (according to the activities of the central engines of LGRBs are able to arrive within thousands of seconds), and the precession period  $T$  is set as 10 s to satisfy the condition that the precession period is much less than the active timescale of the central engine. Note that  $t_{\text{end}}$  and  $T$  are measured in the lab frame. Based on the expected value of the precession angle obtained by Stone et al. (2013), we set the precession angle, i.e.,  $\theta_p = 7^\circ$ . For simplicity, we assume the same values for the dynamical parameters in both cases, including  $L_{\text{ej}} = 10^{49} \text{ erg s}^{-1}$ ,  $\Gamma_{\text{ej}} = 300$ , and  $n_1 = 1 \text{ cm}^{-3}$ , except  $\sigma_{\text{ej}} = 10^{-1}$  in Case I and  $10^{-3}$  in Case II. Meanwhile, the emission parameter values are as follows:  $\varepsilon_{e,2} = 10^{-1}$ ,  $\varepsilon_{B,2} = 10^{-3}$ , and  $p_2 = p_3 = 2.5$  in both cases, excluding  $\varepsilon_{e,3} = 10^{-1}$  in Case I and  $10^{-3}$  in Case II, where  $\varepsilon_{e,2}$  ( $\varepsilon_{e,3}$ ) is the fraction of the internal energy density in the FS (RS) downstream that goes into the electrons and  $p_2$  ( $p_3$ ) is the power-law index of the energy distribution of the shock-accelerated electrons in the FS (RS) downstream. Moreover, here, we fix the linear PD  $\Pi_0 = 0.6$  in the ordered magnetic field, the orientation of the aligned

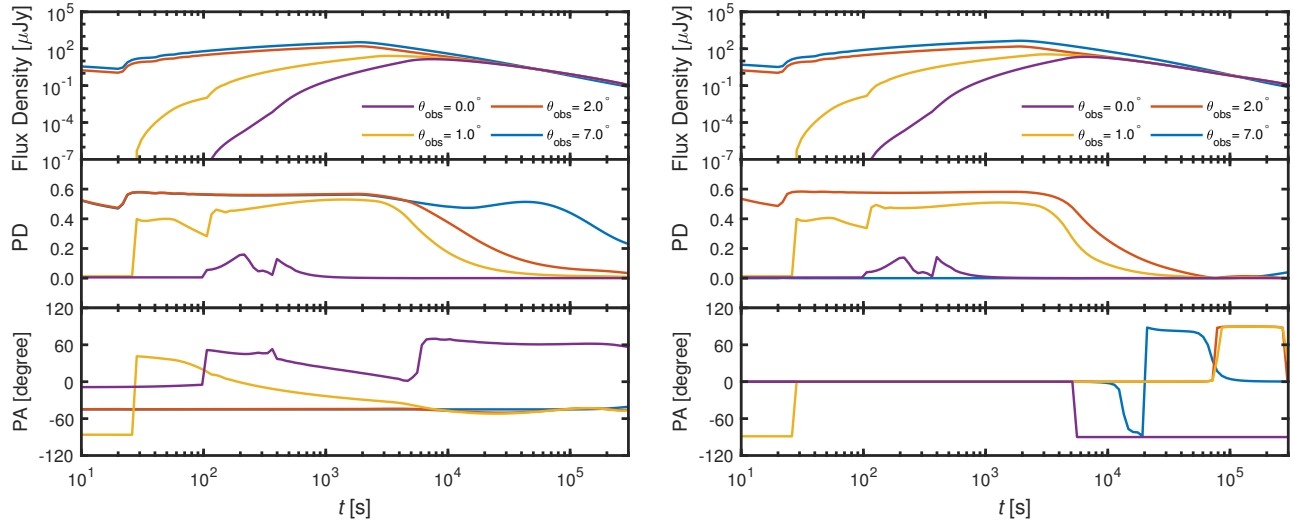


**Figure 2.** Light curves and polarization evolution of GRB early optical afterglows in Case I. The left and right panels show the results with aligned and toroidal magnetic fields in Region 3, respectively, where Region 3 corresponds to the RS emission. The upper, middle, and bottom panels exhibit the light curves and the time evolution of the PD and PA, respectively. The violet, yellow, magenta, and blue lines denote the results obtained for  $\theta_{\text{obs}} = 0^\circ, 1^\circ, 2^\circ,$  and  $7^\circ$ , respectively.

magnetic field  $\delta = \pi/4$ , and the typical redshift  $z = 1$ . All parameters can be found in Table 1.

#### 4.1. Case I

Figure 2 shows the results for Case I (the ordered magnetic field dominates). Noted that the ordered magnetic field all exists in Region 3, which corresponds to the RS emission. The left and right panels correspond to the aligned and toroidal magnetic field configurations in Region 3, respectively (Spruit et al. 2001). The upper, middle, and bottom panels exhibit the light curves and the time evolution of the PD and PA, respectively. The violet, yellow, magenta, and blue lines denote the results obtained for  $\theta_{\text{obs}} = 0^\circ, 1^\circ, 2^\circ,$  and  $7^\circ$ , respectively. Here,  $\theta_{\text{obs}}$  is the angle between the precession axis and the line of sight, as shown in Figure 1.

The magnetic field topology has little influence in shaping the optical light curves (see the upper panels of Figure 2), whose emission approximately peaks at thousands of seconds post-burst. The hardly low fluxes for the light curves with  $\theta_{\text{obs}} = 0^\circ$  and  $1^\circ$  in the early time are due to the delayed arrivals of the synchrotron photons as the line of sight deviates from the path of the jet precession. The light curves with  $\theta_{\text{obs}} = 2^\circ$  and  $7^\circ$  have significantly higher fluxes in the early time because the line of sight points to the path of jet precession for  $\theta_{\text{obs}} = 2^\circ$  and  $7^\circ$ , which correspond the cases of the lines of sight on the edge and inside of the subjects, respectively. Additionally, the peak fluxes with  $\theta_{\text{obs}} = 0^\circ$  are approximately one order of magnitude lower than those with  $\theta_{\text{obs}} = 7^\circ$  due to the assumption of a top-hat jet for which the peak fluxes sharply decline when the

line of sight moves from the inside to the outside of the precessing jets. This implies that the precession angle should not be too large, otherwise, a much lower flux will be undetectable (Laskar et al. 2015).

For the cases with  $\theta_{\text{obs}} = 0^\circ$ , the PDs (middle panels) are almost zero, regardless of the magnetic field configurations, which indicates that the high polarization produced in the ordered magnetic field can be almost counteracted in the precession process. However, for other values of  $\theta_{\text{obs}}$ , high PDs appear. Once  $\theta_{\text{obs}} = 7^\circ$ , the PD reaches approximately 60% in the aligned magnetic field configuration, whereas the value of the PD is close to zero in the toroidal configuration (Lyutikov et al. 2003). These results suggest that the effect of jet precession on the PD strongly depends on the position of the line of sight, namely, it is obvious only when the line of sight is around the precession axis. Here, the irregular shapes of the evolution profiles of the PD in the early time should arise from the assumption made for the dynamics, but these have no significant effect on the overall evolutionary trend of the PD.

For the PA (bottom panels), its evolution is characterized by basically constant, gradual decay, and abrupt changes. First, the constant evolution, such as that presented in the results obtained for  $\theta_{\text{obs}} = 7^\circ$  with the aligned magnetic field configuration, is attributed to the invariant direction of the ordered magnetic field in the visible core (i.e., the  $1/\Gamma$  core). Second, the gradual decay, in the situation for  $\theta_{\text{obs}} = 1^\circ$  with the aligned magnetic field configuration, occurs when the direction of the ordered magnetic field in the visible core gradually changes due to the increase in the observational

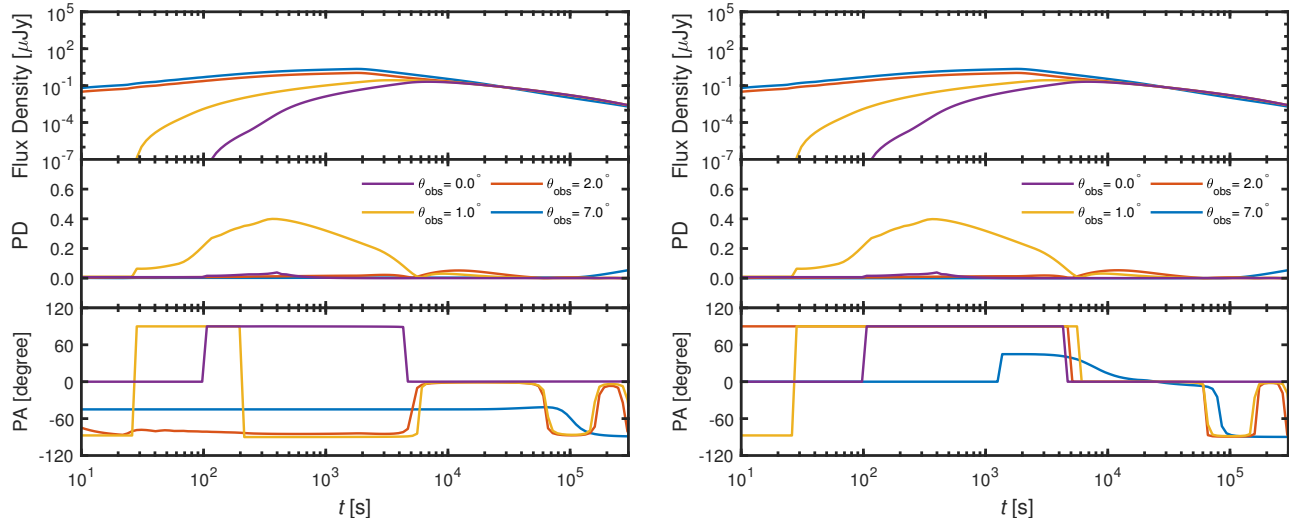


**Figure 3.** Light curves and polarization evolution of GRB early optical afterglows that are the same as those in Figure 2 but for Case II.

regions of the subjects moving in different positions with the decrease Lorentz factors. Third, the appearance of the abrupt changes, including both the abrupt changes for  $90^\circ$  and  $180^\circ$ , depends on the transition of the signs of  $Q_{\nu_{\text{obs}}}^X$  or  $U_{\nu_{\text{obs}}}^X$ , reflecting the abrupt changes in the direction of the ordered magnetic field. When the sign of  $Q_{\nu_{\text{obs}}}^X$  changes, abrupt changes in  $90^\circ$  occur. In contrast, when the sign of  $U_{\nu_{\text{obs}}}^X$  changes with  $Q_{\nu_{\text{obs}}}^X < 0$ , abrupt changes in  $180^\circ$  appear, as shown in the results obtained for  $\theta_{\text{obs}} = 7^\circ$  with the toroidal magnetic field configuration. Therefore, which of these features appears mainly depends on how the direction of the ordered magnetic field in the visible core changes.

#### 4.2. Case II

Figure 3 shows the results obtained for Case II (the random magnetic field dominates). Here, Case II corresponds the dominance of the FS emission because the random magnetic field exists in Region 2. The left and right panels still correspond to the aligned and toroidal magnetic field configurations in Region 3, respectively.

One can find that the light curves and the evolutions of the PD in both panels maintain consistency. Meanwhile, the values of the PDs are significantly low, except in the situation of  $\theta_{\text{obs}} = 1^\circ$ . In the situation of  $\theta_{\text{obs}} = 0^\circ$ , the PDs are almost zero, which is due to the jet precession.

The evolution of PAs appears to be more complex. Most of the evolution profiles exhibit irregularly abrupt changes over two times, which suggests that the direction of the total magnetic fields is irregularly changeable. This should be attributed to the irregular changes in the geometry of the emission region in the visible core with a decrease in the Lorentz factors. In addition, since the signs of  $Q_{\nu_{\text{obs}}}^X$  and  $U_{\nu_{\text{obs}}}^X$  with significantly small values

are sensitive to the mathematical definition, related features for the PAs should be treated carefully.

## 5. SUMMARY

It is expected that jet precessions exist in GRBs, and polarimetry plays an important role in the study of GRBs. These results motivate interest in determining whether the jet precession can significantly affect the polarization behavior, especially in the early optical afterglows. Consequently, we investigate the polarization evolution of early optical afterglows in the framework of long-lived precessing jets with either dominant ordered magnetic field or random component (i.e. scenarios with mixed properties). As a result, we find that the high levels of PDs expected in the RS emission, due to the large-scale magnetic fields ejected from the central engine, can be significantly reduced by the jet precession.

In our model, the depolarizing effect induced by the jet precession still exists for the cases with other different active timescales of the central engines and the precession periods. For the case with more precession laps in an engine active timescale, the depolarizing effect might be more significant. Moreover, the decreasing precession angle should increase the polarizing effect.

Recently, GRB 190114C, the first TeV-detected GRB (MAGIC Collaboration et al. 2019), is reported to have a low PD,  $\sim 2\% - 7\%$ , in its early afterglows, and the low PD can be well explained by the large-scale magnetic fields distorted before the RS emission (Jordana-Mitjans et al. 2020, and references therein). Actually, the low PD of the early afterglow of GRB 190114C can also be interpreted by the depolarizing effect in jet precession model.

In addition to the early afterglows, low PDs can be detected in the prompt  $\gamma$ -ray emission (Zhang et al. 2019; Kole et al. 2020). Zhang et al. (2019) reported a sample of polarization measurements obtained using the dedicated GRB polarimeter (POLAR) and obtained an average PD,  $\sim 10\%$ , which is lower than that predicted by some popular models. Lan et al. (2021) proposed that these results can be explained by a model involving a mixed magnetic field (i.e., by entangling the large-scale ordered component present in the ejecta). However, the origin of the mixed magnetic fields is still unclear. Inspired by our results, we suspect that jet precession is a plausible mechanism for building mixed magnetic fields. For example, in the framework of the massive collapsars, due to the high accretion rate and the redistribution of

the fallback debris during the first few to tens of seconds, the precession of the jets should be quite fast, violent and even irregular (Liu et al. 2018; Huang & Liu 2021). This will lead to a distortion of the large-scale ordered magnetic fields.

## ACKNOWLEDGMENTS

We thank the anonymous referee for helpful suggestions and comments. This work was supported by the National Natural Science Foundation of China under grants 12173031 and 11822304, and the science research grants from the China Manned Space Project with No. CMS-CSST-2021-B11.

## REFERENCES

- Ai, S. & Zhang, B. 2021, *MNRAS*, 507, 1788.  
doi:10.1093/mnras/stab2000
- Begelman, M. C., Blandford, R. D., & Rees, M. J. 1984, *Reviews of Modern Physics*, 56, 255.  
doi:10.1103/RevModPhys.56.255
- Beloborodov, A. M. & Uhm, Z. L. 2006, *ApJL*, 651, L1.  
doi:10.1086/508807
- Blackman, E. G., Yi, I., & Field, G. B. 1996, *ApJL*, 473, L79. doi:10.1086/310403
- Buckley, D. A. H., Bagnulo, S., Britto, R. J., et al. 2021, *MNRAS*, 506, 4621. doi:10.1093/mnras/stab1791
- Burrows, D. N., Kennea, J. A., Ghisellini, G., et al. 2011, *Nature*, 476, 421. doi:10.1038/nature10374
- Chen, Q. & Liu, X.-W. 2021, *MNRAS*, 504, 1759.  
doi:10.1093/mnras/stab946
- Covino, S. & Gotz, D. 2016, *Astronomical and Astrophysical Transactions*, 29, 205
- Dai, Z. G. & Lu, T. 1998a, *A&A*, 333, L87
- Dai, Z. G. & Lu, T. 1998b, *PhRvL*, 81, 4301.  
doi:10.1103/PhysRevLett.81.4301
- Deng, W., Zhang, B., Li, H., et al. 2017, *ApJL*, 845, L3.  
doi:10.3847/2041-8213/aa7d49
- Geng, J.-J., Huang, Y.-F., Wu, X.-F., et al. 2018, *ApJ*, 862, 115. doi:10.3847/1538-4357/aacd05
- Giannios, D., Mimica, P., & Aloy, M. A. 2008, *A&A*, 478, 747. doi:10.1051/0004-6361:20078931
- Gill, R., Kole, M., & Granot, J. 2021, *Galaxies*, 9, 82.  
doi:10.3390/galaxies9040082
- Gorbovskey, E. S., Lipunov, V. M., Buckley, D. A. H., et al. 2016, *MNRAS*, 455, 3312. doi:10.1093/mnras/stv2515
- Granot, J. & Königl, A. 2003, *ApJL*, 594, L83.  
doi:10.1086/378733
- Hou, S.-J., Du, S., Liu, T., et al. 2021, *ApJ*, 922, 102.  
doi:10.3847/1538-4357/ac2c74
- Hou, S.-J., Liu, T., Gu, W.-M., et al. 2014, *ApJL*, 781, L19.  
doi:10.1088/2041-8205/781/1/L19
- Huang, B.-Q., Lin, D.-B., Liu, T., et al. 2019, *MNRAS*, 487, 3214. doi:10.1093/mnras/stz1426
- Huang, B.-Q. & Liu, T. 2021, *ApJ*, 916, 71.  
doi:10.3847/1538-4357/ac07a0
- Huang, Y. F. & Cheng, K. S. 2003, *MNRAS*, 341, 263.  
doi:10.1046/j.1365-8711.2003.06430.x
- Huang, Y. F., Dai, Z. G., & Lu, T. 1999, *MNRAS*, 309, 513. doi:10.1046/j.1365-8711.1999.02887.x
- Jordana-Mitjans, N., Mundell, C. G., Kobayashi, S., et al. 2020, *ApJ*, 892, 97. doi:10.3847/1538-4357/ab7248
- Jordana-Mitjans, N., Mundell, C. G., Smith, R. J., et al. 2021, *MNRAS*, 505, 2662. doi:10.1093/mnras/stab1003
- King, O. G., Blinov, D., Giannios, D., et al. 2014, *MNRAS*, 445, L114. doi:10.1093/mnras/slu149
- Kole, M., De Angelis, N., Berlato, F., et al. 2020, *A&A*, 644, A124. doi:10.1051/0004-6361/202037915
- Lan, M.-X., Geng, J.-J., Wu, X.-F., et al. 2019a, *ApJ*, 870, 96. doi:10.3847/1538-4357/aaf41d
- Lan, M.-X., Wu, X.-F., & Dai, Z.-G. 2016, *ApJ*, 816, 73.  
doi:10.3847/0004-637X/816/2/73
- Lan, M.-X., Wu, X.-F., & Dai, Z.-G. 2018, *ApJ*, 860, 44.  
doi:10.3847/1538-4357/aac26e
- Lan, M.-X., Wu, X.-F., & Dai, Z.-G. 2021, *Research in Astronomy and Astrophysics*, 21, 055.  
doi:10.1088/1674-4527/21/3/055
- Lan, M.-X., Xue, R., Xiong, D., et al. 2019b, *ApJ*, 878, 140.  
doi:10.3847/1538-4357/ab21ce
- Laskar, T., Berger, E., Margutti, R., et al. 2015, *ApJ*, 814, 1. doi:10.1088/0004-637X/814/1/1

- Laskar, T., Alexander, K. D., Gill, R., et al. 2019, *ApJL*, 878, L26. doi:10.3847/2041-8213/ab2247
- Lazzati, D. 2006, *New Journal of Physics*, 8, 131. doi:10.1088/1367-2630/8/8/131
- Li, A., Zhang, B., Zhang, N.-B., et al. 2016, *PhRvD*, 94, 083010. doi:10.1103/PhysRevD.94.083010
- Liu, T., Gu, W.-M., & Zhang, B. 2017a, *NewAR*, 79, 1. doi:10.1016/j.newar.2017.07.001
- Liu, T., Liang, E.-W., Gu, W.-M., et al. 2010, *A&A*, 516, A16. doi:10.1051/0004-6361/200913447
- Liu, T., Lin, C.-Y., Song, C.-Y., et al. 2017b, *ApJ*, 850, 30. doi:10.3847/1538-4357/aa92c4
- Liu, T., Song, C.-Y., Zhang, B., et al. 2018, *ApJ*, 852, 20. doi:10.3847/1538-4357/aa9e4f
- Lu, J.-F. 1990, *A&A*, 229, 424
- Lyutikov, M., Pariev, V. I., & Blandford, R. D. 2003, *ApJ*, 597, 998. doi:10.1086/378497
- Ma, X., Tao, L., Zhang, S.-N., et al. 2021, *Nature Astronomy*, 5, 94. doi:10.1038/s41550-020-1192-2
- MAGIC Collaboration, Acciari, V. A., Ansoldi, S., et al. 2019, *Nature*, 575, 455. doi:10.1038/s41586-019-1750-x
- Margon, B. 1984, *ARA&A*, 22, 507. doi:10.1146/annurev.aa.22.090184.002451
- Miley, G. 1980, *ARA&A*, 18, 165. doi:10.1146/annurev.aa.18.090180.001121
- Mundell, C. G., Kopač, D., Arnold, D. M., et al. 2013, *Nature*, 504, 119. doi:10.1038/nature12814
- Nakar, E. 2007, *PhR*, 442, 166. doi:10.1016/j.physrep.2007.02.005
- Nava, L., Sironi, L., Ghisellini, G., et al. 2013, *MNRAS*, 433, 2107. doi:10.1093/mnras/stt872
- Portegies Zwart, S. F., Lee, C.-H., & Lee, H. K. 1999, *ApJ*, 520, 666. doi:10.1086/307471
- Proctor, D. D. 2011, *ApJS*, 194, 31. doi:10.1088/0067-0049/194/2/31
- Reynoso, M. M., Romero, G. E., & Sampayo, O. A. 2006, *A&A*, 454, 11. doi:10.1051/0004-6361:20054564
- Rossi, E. M., Lazzati, D., Salmonson, J. D., et al. 2004, *MNRAS*, 354, 86. doi:10.1111/j.1365-2966.2004.08165.x
- Rybicki, G. B., & Lightman, A. P. 1979, *Radiative processes in astrophysics* (New York: Interscience)
- Sari, R. 1999, *ApJL*, 524, L43. doi:10.1086/312294
- Sari, R., Piran, T., & Narayan, R. 1998, *ApJL*, 497, L17. doi:10.1086/311269
- Shimoda, J. & Toma, K. 2021, *ApJ*, 913, 58. doi:10.3847/1538-4357/abf2c2
- Spruit, H. C., Daigne, F., & Drenkhahn, G. 2001, *A&A*, 369, 694. doi:10.1051/0004-6361:20010131
- Steele, I. A., Kopač, D., Arnold, D. M., et al. 2017, *ApJ*, 843, 143. doi:10.3847/1538-4357/aa79a2
- Steele, I. A., Mundell, C. G., Smith, R. J., et al. 2009, *Nature*, 462, 767. doi:10.1038/nature08590
- Stone, N., Loeb, A., & Berger, E. 2013, *PhRvD*, 87, 084053. doi:10.1103/PhysRevD.87.084053
- Sun, M.-Y., Liu, T., Gu, W.-M., et al. 2012, *ApJ*, 752, 31. doi:10.1088/0004-637X/752/1/31
- Tarnopolski, M. & Marchenko, V. 2021, *ApJ*, 911, 20. doi:10.3847/1538-4357/abe5b1
- Toma, K., Sakamoto, T., Zhang, B., et al. 2009, *ApJ*, 698, 1042. doi:10.1088/0004-637X/698/2/1042
- Usov, V. V. 1992, *Nature*, 357, 472. doi:10.1038/357472a0
- Woosley, S. E. & Bloom, J. S. 2006, *ARA&A*, 44, 507. doi:10.1146/annurev.astro.43.072103.150558
- Wu, X. F., Dai, Z. G., Huang, Y. F., et al. 2005, *MNRAS*, 357, 1197. doi:10.1111/j.1365-2966.2005.08685.x
- Zhang, B. 2018, *The Physics of Gamma-Ray Bursts* (Cambridge: Cambridge Univ. Press)
- Zhang, B., Fan, Y. Z., Dyks, J., et al. 2006, *ApJ*, 642, 354. doi:10.1086/500723
- Zhang, B. & Kobayashi, S. 2005, *ApJ*, 628, 315. doi:10.1086/429787
- Zhang, B. & Mészáros, P. 2001, *ApJL*, 552, L35. doi:10.1086/320255
- Zhang, B. & Yan, H. 2011, *ApJ*, 726, 90. doi:10.1088/0004-637X/726/2/90
- Zhang, S.-N., Kole, M., Bao, T.-W., et al. 2019, *Nature Astronomy*, 3, 258. doi:10.1038/s41550-018-0664-0
- Zhang, W. & MacFadyen, A. 2009, *ApJ*, 698, 1261. doi:10.1088/0004-637X/698/2/1261